High-resolution, Earth-like Rayleigh number viscoplastic spherical convection models

Zel Hurewitz, Lukas Fuchs, Thorsten Becker

May 2019

Abstract

The self-consistent generation of realistic plate tectonics from mantle convection is a long-standing problem in geophysics. In this paper, I will demonstrate how improvements in computational mantle convection simulations allow for more realistic plate-like metrics. I run the finite-element code CitcomS on a spherical annular domain to study incompressible, viscoplastic mantle convection for Earth-like planets. I perform high-resolution runs to investigate constant yield stress models at high mantle Rayleigh numbers from 10^6 to 10^8 and with a viscosity contrast of 10^5. I find no episodic models for $\Delta\eta = 10^5$ and find also that the plate-like/stagnant transition remains at a 60-80 MPa independent of Ra, lower than the $\Delta\eta = 10^4$ transition of 150-250 MPa in Ref [FB09]. I further find that the toroidal-poloidal ratio increases as a function of Ra, averaging 0.5-0.6 for some models, higher than the 0.4-0.5 seen in previous works [FB09][Tac00b]. Plateness does not increase significantly with either viscosity contrast or Ra.

1 Introduction

Work has been done over the last few decades to understand the physical processes which give rise to plate tectonics, the motion of rigid plates on the Earth's surface over timescales of hundreds of millions of years. Despite being well understood as the surface expression of convection of the mantle, plate tectonics is difficult to recreate in numerical models self-consistently, i.e. without direct imposition of faults at boundaries. The complexity of the Earth system gives rise to behaviour unlike simple viscous convection, including a great deal strike-slip (horizontal, not converging or diverging) motion and one-sided sheet-like downwellings, as opposed to the symmetric downwellings often seen in models. The viscosity law (rheology) of the rock almost fully determines the style of convection.

In this paper, I try to balance the relevance of the mantle convection problem to the Earth and similar planets against the desire to produce broadly applicable results. To that end, the models presented here are simplified compared to the

Earth system. For most parameters I use Earth-like values, except when in conflict with numerical limitations. However, the rock rheology is simplified. In this way, the generic nature of mantle convection can be studied without the results being overly specific to the Earth itself. Despite these limitations, numerical modeling of mantle convection is widely agreed to be a valid method of research [Tac00b]. Numerical models allow the test of hypotheses about the underlying physics of convection. The physical basis of the governing equations and the success of recreating behaviour similar to the real world supports the use of models.

2 Model Setup and Equations of Motion

I use the incompressible viscoplastic finite-element convection code CitcomS to solve for conservation of momentum, mass, and energy on a spherical annular domain. I run models with pure internal heating, an Arrhenius viscosity law, and pseudo-plastic yielding to produce plate-like behaviour. I explore a range of Rayleigh numbers, yield stresses, and viscosity contrasts.

2.1 Relationship to Rayleigh-Bénard Convection

Rayleigh-Bénard convection is the general process of fluid convecting heat from a warm base to a cold top. It is described by coupling the conservation of mass and momentum in the Navier-Stokes equations to the conservation of energy in the heat equation. The Navier-Stokes equations are a set of partial differential equations which describe the continuum motion of fluids. They encapsulate processes ranging from velocity advection to Coriolis acceleration and are in general very difficult to solve analytically and numerically. Fortunately for our purposes, the mantle flows very slowly and operates under the infinite-Prandtl number assumption. The Prandtl number results from the non-dimensionalization of the Navier-Stokes equations and is defined as the ratio of momentum diffusivity to thermal diffusivity. The infinite-Prandtl number assumption is the limit of the Boussinesq approximation (eq. 3) to standard Rayleigh-Bénard convection and implies a negligible Reynolds number [Wan04]. This means the velocity field is entirely dependent on the temperature field [DC01] and that velocity advection and Coriolis forces can be neglected [Wan04][DC01].

2.2 Stokes Flow

By assuming the Prandtl number to be infinite, the Navier-Stokes equations reduce to the Stokes equation (eq. 1), which models creeping flow [Mor+14] [Ric07][ZGM98]. In this treatment, I ignore the compressibility of the mantle, leading to the second equation, which states that the divergence of the velocity field is zero (eq. 2).

$$-\nabla P + \nabla \cdot \left(\eta(\nabla \mathbf{u} + \nabla \mathbf{u}^{\mathbf{T}} - \frac{2}{3}(\nabla \cdot \mathbf{u})\mathbf{I})\right) - \Delta\rho g \hat{\mathbf{r}} = 0 \tag{1}$$

$$\nabla \cdot \mathbf{u} = 0 \tag{2}$$

The Stokes equation can also be derived from a balance of forces acting on a small fluid parcel in the mantle [Ric07]. The pressure gradient force (left) is balanced by the viscous stress (middle) and the buoyancy forces (right). The Stokes is a linear equation and admits an instantaneous solution which is satisfied at all times. Solutions to the Stokes equation are non-turbulent, which means that they can be adequately resolved without parameterizing turbulent eddies.

In general, the Stokes equation is dependent on the temperature field through the buoyancy and viscosity terms. The viscosity is taken to be temperature dependent [FB09][Tac00b].

2.3 Heat Equation

However, the Stokes equation does not exist in isolation. The buoyancy of fluid parcels is dependent on the temperature. In this case, the linear Boussinesq approximation (eq. 3) to the compressibility of materials is applied, so the buoyancy is linear with the excess temperature above the adiabat $T - \bar{T}_a$ [Wan04][DC01][FB09][Mor+14]. Here, α is the compressibility constant, $\bar{\rho}$ is the reference density along the adiabat, and $\Delta\rho$ is the excess buoyancy.

$$\Delta\rho = -\alpha\bar{\rho}(T - \bar{T}_a) \tag{3}$$

The temperature field evolves according to the heat equation (eq. 4), which can be derived from local conservation of energy [Ric07]. The equation describes how change in temperature of a fluid parcel, as you are advected along with it (left term), is governed by the diffusion of heat (middle term) and a handful of source terms. Here ρ is the density, c_P the heat capacity, and κ the diffusivity.

$$\rho c_P \left(\frac{\partial T}{\partial t} + \mathbf{u} \cdot \nabla T\right) = \rho c_P \kappa \nabla^2 T - \rho\alpha g(\mathbf{u} \cdot \hat{\mathbf{r}})T + \Phi + \rho Q \tag{4}$$

Non-linearity enters the picture for the first time with the coupling of the heat equation to Stokes flow in the velocity advection and viscous dissipation terms, which are both dependent on the Stokes solution. Solutions to the combined equations will no longer be linear and time-independent, and indeed will show a great deal of time dependence and variability [Ric07].

There are a few important source terms in the heat equation. $\Phi = \epsilon : \sigma$ is the double tensor contraction of the strain and stress tensors and represents viscous-dissipation, the frictional work done by the mantle released as heat. The adiabatic term $-\rho\alpha g(\mathbf{u} \cdot \hat{\mathbf{r}})T$ in the heat equation represents the temperature

change caused by a fluid parcel rising or falling in the mantle. The release of pressure on a rising fluid parcel allows it to expand and cool adiabatically [Ric07][Mor+14]. In this treatment, latent heat is ignored, as there are no phase changes implemented. Finally, there is the radiogenic source term ρQ, explained in detail in a later section.

2.4 Rayleigh Number

The Rayleigh number comes from a non-dimensionalization of the buoyancy term in the Stokes equation. It is defined like in equation 5 as the ratio of the heat transported by advection as by conduction [Tac00b][Ric07]. Rayleigh number is effectively a proxy for the vigor of convection.

$$Ra_D = \frac{\rho g \alpha g \Delta T D^3}{\eta_0 \kappa} \tag{5}$$

Here, ρ, g, α, ΔT, D, η_0, and κ are the reference density, reference gravity, compressibility, temperature drop, mantle depth, reference viscosity, and diffusivity respectively. The Rayleigh number in CitcomS is given with the planet radius [Mor+14] instead of the mantle depth. The radius Rayleigh number Ra_R, which I mostly refrain from using in this paper to maintain continuity with Refs [FB09][Tac00b], is converted to the mantle Rayleigh number Ra_D using the following equation, where R is the radius.

$$Ra_D = \frac{D^3}{R^3} Ra_R \approx \frac{Ra_R}{10.97} \tag{6}$$

2.5 Boundary Conditions

The boundary conditions are critical for determining the model's behaviour. I take the top and bottom velocity conditions for the Stokes equation as free-slip, meaning that there is no horizontal stress imposed. The top temperature condition is an isothermal cold non-dimensional temperature of zero. This feature mimics the frigidity of the surface of the Earth compared to the mantle. The surface temperature varies on too short an timescale and with too small an amplitude to investigate those effects here.

The bottom temperature boundary condition defines two classes of models. A bottom-heated model passes heat through the core at the core-mantle boundary (CMB). This can be accomplished either with a Dirichlet constant temperature (of one), or a Neumann constant heat flux, or both. The mantle flow in this case is a mixture of upwelling and downwelling and there are large temperature gradients at the top and bottom of the mantle. The concentration of heat in the relatively small volume directly surrounding the core generates rapidly rising plumes. There are thought to be analogs to these model plumes on Earth which create hotspots at the surface [DR92].

Plumes may be important to mantle flow in the real world. For instance, they carry approximately 20-40% of the internal heat of the Earth to the surface [JLM07][LHB08]. Hot spots are correlated with divergent plate boundaries [Zha04] and may guide their formation. The largest plumes derive from the the CMB, although there is evidence of small-scale ones originating in the mid-mantle [Zha04].

However, hot spots comprise a small fraction of the Earth's surface area and likely a small fraction of the mantle volume as well [Zha04][BKI15]. They are small-wavelength phenomena which I treat as perturbations to a broader mantle flow generated by internal radiogenic heating [DR92]. I have found, along with Ref [FB09], that numerical plumes destroy plates and exert a disproportionate amount of influence on surface structure at these resolutions. This finding is not uniform, as Ref [CGU17], using a high-resolution model, found that plumes sometimes interacted with ridges without destroying the plates. In these models I neglect the contribution of plumes to the flow pattern and study only purely internally heated models with no basal heat flux. Internally-heated models generate heat uniformly throughout the bulk of the mantle. They show only downwellings and have a flat temperature gradient from the CMB until the lower lithosphere, the top, strong layer of the Earth.

2.6 Internal Heating

The internal heat generation of the rock itself is the source term Q in the heat equation. Although theoretically, Q may find its origin from any process, the dominant components are radiogenic and primordial heat [DR92]. In the real world, this source is a function of position, and especially time, as natural radioactivity declines exponentially with the age of the rock. Most radioactivity in the mantle today comes from uranium-235 and thorium-232 [JLM07]. At early times in the Earth's history, closer to the formation of the Solar System, other elements like potassium were more prevalent, but their relatively short half-lives have reduced their contribution [JLM07]. In this treatment, the internal heating rate is held to be uniform and constant in order to study steady-state convection.

2.7 Arrhenius Viscosity Law

The dominant control over the style of flow in the mantle is the rheology, the treatment of the viscosity. An isoviscous mantle, in which the viscosity is spatially uniform, leads to unphysically broad surface deformation.

$$\eta(T) = \eta_0 \exp\left(\frac{E_\eta}{T + T_\eta} - \frac{E_\eta}{1 + T_\eta}\right) \tag{7}$$

$$E_\eta = \ln(\Delta\eta)(T_\eta + T_\eta^2) \tag{8}$$

The viscosity of mantle rock is highly temperature dependent. In the same way that warmed honey flows more fluidly, rock viscosity has a strongly expo-

nential creep behaviour over such this large range of temperatures, set by the melting temperature of the mantle rock ($\approx 300 - 1600$ K [Tac00b]). The viscosity follows an Arrhenius law (eq. 7) where E_η is the activation energy of the creeping flow (properly activation temperature, when non-dimensionalized in this manner) and T_η is the offset temperature which controls the non-linearity. In this experiment, T_η is unity. The activation energy E_η is chosen to ensure the viscosity varies between 1 (T=0) and $\Delta\eta$ (T=1) by equation 8. It depends only on the viscosity contrast $\Delta\eta$, which is chosen to be either 10^4 ($E_\eta = 18.43$) [FB09] or 10^5 ($E_\eta = 23.03$) [Tac00b].

There are two dominant power-law creeping mechanisms in Earth's mantle. Dislocation creep involves the propagation of dislocations, or discontinuities, within the crystal lattice, and does not depend on the size of the crystalline grains within the rock. Diffusion creep is the diffusion of holes within the crystalline lattice and is grain-size dependent [Ric07]. The two mechanisms have different activation energies for olivine [FB17]. However, a full treatment of the implementation of these laws would be against the design of this paper, as it would both complicate the models and also make them less broadly relevant. Furthermore, Newtonian temperature dependent convection can return results similar to power-law convection [Chr84]. Therefore I choose a constant activation energy for the whole mantle, which is significantly lower than either that of diffusion or dislocation creep, for computational reasons.

The Arrhenius law is often linearized into the Frank-Kamenetskii approximation for mantle simulations. Work has been done on the difference between the two and found that the Arrhenius formulation gives more realistic thin lithospheres [SH13]. My treatment uses the full Arrhenius dependence. The temperature offset is low (unity), however, which results in a law close to the linearization.

The effect of adding a temperature dependence to the viscosity is to the seal the surface of the planet into a stagnant lid. The surface is cold, leading to a highly viscous, strong lithosphere. The strength of the cold rock prevents any motion at all. Deformation is very limited, and there is no surface structure similar to Earth's plate tectonics [FB09][MS98][Sol95][Chr84][OSZ91][Tac00a] [Tac00b].

2.8 Pseudo-Plastic Yielding

The cornerstone of the theory of plate tectonics is the presence of strong plates with weak plate boundaries which permit relative motion of the plates. I accomplish fracture of the surface by adding a plasticity term to the viscosity law [FB09]. Essentially, at higher strain rates, the rock experiences Byerlee-style faulting and shear zones and slides with less resistance, which results in a lower viscosity [MS98]. Although microphysical laws empirically determined from laboratory experiments can be applied, the essential behaviour is captured by a pseudo-plastic rheological law [Tac00b].

$$\eta_y(\dot{\epsilon}) = \sigma_y / 2\dot{\epsilon}_{II} \tag{9}$$

$$\eta_{eff}(T, \dot{\epsilon}) = \frac{1}{\frac{1}{\eta(T)} + \frac{1}{\eta_y(\dot{\epsilon})}} \tag{10}$$

$$\dot{\epsilon}_{II} = \sqrt{\frac{1}{2} \sum_{ij} \dot{\epsilon}_{ij}^2} \tag{11}$$

The viscosity decreases with the second invariant of the strain rate tensor (eq. 11) according to equation 14. The rate of viscosity decrease depends on the yield stress σ_y. This formulation is a proxy for a large number of physical mechanisms [FB09]. The effective viscosity is the lower of the two viscosities $\eta(T)$ and $\eta_y(\dot{\epsilon}_{II})$. Although a simple minimum law can be applied [Tac00b], I apply a smoother harmonic minimum law (eq. 10).

2.9 Scaling and Non-Dimensionalization

The equations presented here are non-dimensionalized to aid numerical simulation and reduce the number of apparent material parameters [Mor+14]. I show the scalings in the following equations with parameters chosen in Table 1. The tildes represent non-dimensional quantities.

Time is scaled like equation 12. Equation 13 defines η_0, the reference viscosity, which I choose to be Rayleigh-number dependent in the manner following [FB09]. The dimensional yield stress is presented in equation 14. It is dependent on the Rayleigh number.

$$t = \frac{R^2}{\kappa} \tilde{t} \approx 1287 \text{ Ga} \cdot \tilde{t} \tag{12}$$

$$\eta_0 = 10^{23} \frac{10^6}{Ra_R} \tag{13}$$

$$\sigma_y = \frac{\eta_0 \kappa}{R^2} \tilde{\sigma}_y = 2423 \text{ MPa} \cdot \frac{\tilde{\sigma}_y}{Ra_R} \tag{14}$$

Variable	Meaning	Value
Q	Internal Heating	60 (7 TW)
κ	Diffusivity	10^{-6} m^2/s
ΔT	Temperature Drop	1300 K
R	Radius	6371 km
D	Mantle Depth	2871 km
g	Reference Gravity	10 m/s^2

Table 1: Values for the constants used in this experiment, taken from Refs. [FB09][Tac00b].

2.10 Finite-Element Code

The models are run with the finite element code CitcomS on a spherical annular domain. The code discritizes the domain into finite elements and arranges the temperatures, pressures, and velocities at each node into a vector. It sets up a matrix which describes the discritized differential equations and inverts the matrix against the vector, using a conjugate gradient Uzawa scheme, to get the solution for the next timestep [Zho+07a]. The domain is split into 12 diamond-shaped caps, each of which can run multiple processors in the two horizontal directions and in the vertical. There are multiple nodes and volumes for each processor. The volumes are approximately equal in size [Mor+14].

I use two resolutions in this experiment. The lower has 64^3 volumes per cap for a total of over 3.1 million volumes requiring 192 processors, and the higher has 128^3 volumes per cap, with over 25 million total volumes requiring 768 processors to run effectively. I ran 4 models at low resolution and 15 at the high resolution. I run the models on the Lonestar5 supercomputer located in the Texas Advanced Computing Center in Austin, Texas. $128^3 \times 12$ sized models have been limited in previous works [FB09] by the required memory and processing power and have been relegated to resolution tests [FB09][Tac00b]. I use newly available computing power to run high-resolution models which allows for study of high Rayleigh number and high viscosity contrast models.

The effects of hysteresis are very significant and the thermal evolutionary pathway of the planet is a dominant control over its current state [WL12]. However, I ignore those effects in these models by restarting all of them from one previously run plate-like model.

3 Analysis and Metrics

It is crucial to have more robust methods of analysis than visual inspection. I use three common metrics to help determine the tectonic state of models and measure quantitative changes between models in the same tectonic state.

3.1 Mobility

The simplest metric is mobility, the ratio of the surface velocity and the root-mean-square bulk average velocity of the mantle interior. Plate-like and mobile models tend to have high mobilities, approaching or even in excess of unity. Stagnant models typically have near zero mobility due to the locked and frozen surface [Tac00b][OSZ91].

$$M = v_{rms\_surf}/v_{rms\_bulk} \tag{15}$$

3.2 Toroidal-Poloidal Ratio

The incompressible velocity field on a spherical annular domain can be decomposed using a form of Helmholtz decomposition into a series of spherical harmonics. Unlike scalar fields, vector fields decompose into two families of solutions, toroidal fields and poloidal fields, which sum together to a vector field [Tac00b][BB02] which satisfies the conservation of mass equation. Poloidal vector fields concern vertical overturning within the mantle and are expressed on the surface by divergence and convergence. Toroidal fields are expressed by strike-slip motion at the surface. Earth has a very significant toroidal component to its velocity field [Tac00b][OGH91][A R+93].

$$TPR = \sqrt{\frac{\langle v_{tor}^2 \rangle}{\langle v_{pol}^2 \rangle}} \tag{16}$$

The metric, the toroidal-poloidal ratio (TPR, other papers R_{TP} [Tac00b]), is given by the ratio of the total power in the toroidal field to the total power in the poloidal field (16). I take the powers up to degree 100. The value for the Earth is about 0.5-0.6 over the last 120 Ma [A R+93]. Previous Cartesian-domain models have succeeded in generating TPR values of around 0.4 [Tac00b]. Models in the spherical domain, however, typically exhibit improved toroidal flow[HT08]. Refs. [FB09] and [HT08] managed TPR values for plate-like models up to 0.5.

3.3 Plateness

Plateness is another metric designed to test a model's similarity to Earth-like behaviour [Tac00b]. Plateness is defined by equation 17, below, where f_{80} is the smallest fractional surface area which contains 80% of the total surface strain rate. The theory of plate tectonics maintains that all strain happens at the plate margins, a one-dimensional boundary which has no area. Theoretically then the plateness for the Earth should be exactly unity. Although there is significant deformation in plate interiors, such as along the Tibetan uplift, 80% of the strain generation does occur over narrow (small but finite) margins, resulting in a P value very close to unity [Tac00b][GS92]. The value 0.3 represents f_{80} for a spherical isoviscous model from [FB09], so the plateness is normalized to zero for isoviscous models and reaches 1 at the most plate-like. Unlike Foley et al. [FB09], I do not exclude strain rates under 3% of the maximum, since I did not find them to over-contribute to the strain summation.

$$P = 1 - \frac{f_{80}}{0.3} \tag{17}$$

3.4 Classifying State

I classify models into tectonic state based on the following criteria adapted from previous works [FB09][Tac00b]. Stagnant models have a very low mobility,

below 0.1. Episodic models have a large-amplitude periodic behaviour, which is most distinctive in the bulk average temperature and the mobility, but pervades all the model's metrics. I found no easy way to distinguish mobile and plate-like models, because in the smooth transition between the two, models may have characteristics of both. I choose between the two by visual inspection of the flow fields and surface patterns. Models whose convective flow seemed mostly dominated by drip-like downwellings, I deem mobile, whereas I call models with plate boundaries and more sheet-like downwellings plate-like. Foley et al. [FB09] also suggest that plate-like states can be recognized by a minimum in the standard deviation of mobility compared to mobile and episodic models. I find no episodic models and so cannot apply this finding.

4 Results

4.1 Summary of Models

I use the metrics outlined above to classify the models according to tectonic state. I show the results in the Rayleigh number/yield stress parameter space in Figure 2. I find that the scaled yield stress of the plate-like/stagnant transition is constant with Rayleigh number.

With the four low viscosity contrast ($\Delta\eta = 10^4$) models (Fig. 2), I recreate results described in Foley and Becker [FB09]. I find a plate-like/episodic transition at a yield stress of around 150 MPa and a transition from episodic to stagnant lid at approximately 250 MPa.

I find only no episodic models at a viscosity contrast of 10^5. The overall lack of episodic models holds true not only for those presented in this paper, but also others which I previously studied but are not documented here. This result contrasts with the easily visible episodic models at $\Delta\eta = 10^4$ [FB09]. Furthermore, I find that the transition between plate-like and stagnant models occurs at a yield stress of around 50-60 MPa, significantly lower than the $\Delta\eta = 10^4$ case.

There is not a well-defined transition from the plate-like regime to the mobile regime. As the yield stress decreases, the plate-like downwellings gradually change into the droplet form of pure mobile behaviour. Under 10-20 MPa, however, there is very little resemblance to plate tectonics. Those models are not documented in the phase space below because mobile models take an extraordinarily long model time to reach steady state.

The models exhibit symmetric sheet-like downwellings and do not form pure transform boundaries, but instead mix divergent and transform motion [Tac00a]. The plate boundaries are also broad compared to the Earth [Tac00a]. The convergent margins are thin, but the divergent and strike-slip boundaries are diffuse as shown by [ZGM98] and seen in [FB09][Tac00b].

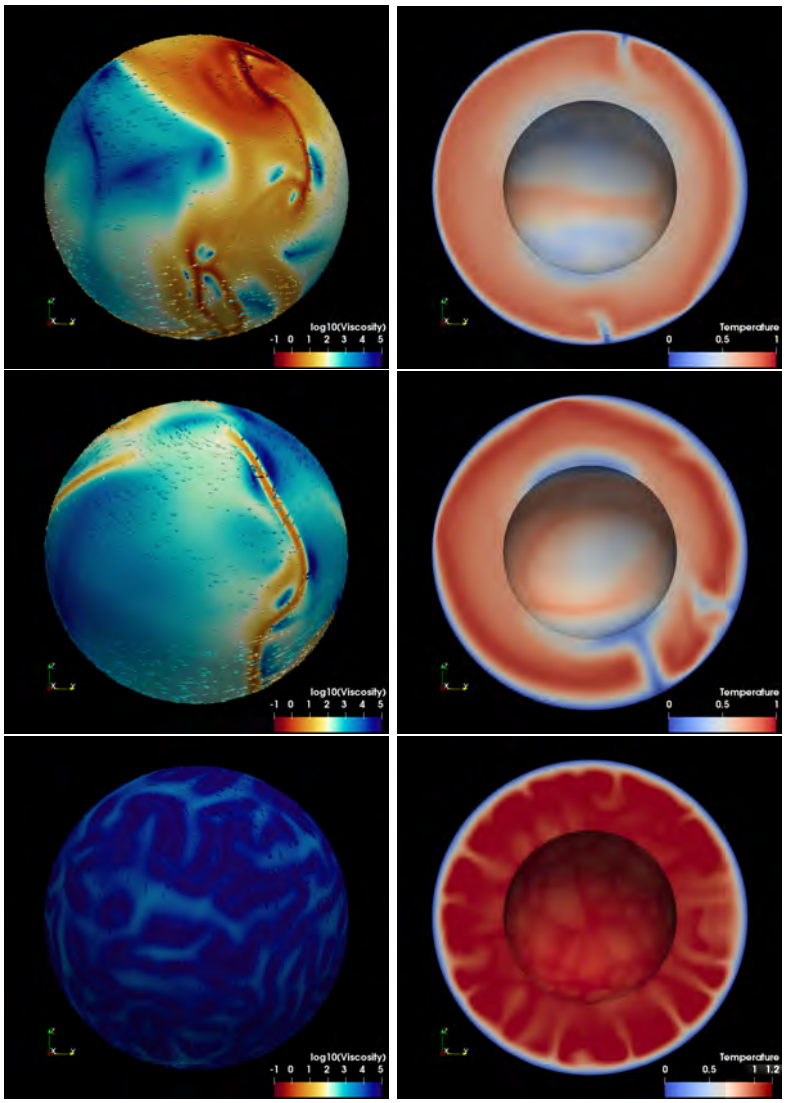

Figure 1: Surface viscosities and velocity vectors (left column) and internal temperature fields (right column) for high-viscosity contrast models ($\Delta\eta = 10^5$, $Ra_D = 10^6$). Since the surface temperature is uniformly zero, the viscosity pattern is entirely due to plastic weakening. The broad deformation on the surface in the top model (24 MPa) indicates that it is approaching the mobile regime, although it is still classified as plate-like. The middle model (60 MPa) is fully plate-like, while the bottom-right (72 MPa) is stagnant. The stagnant model shows the small-wavelength nature of stagnant flow. These flow patterns are typical of models in these tectonic states. Metrics for these models are as follows: top mobility(M)=1.1, plateness(P)=0.85, toroidal-poloidal ratio(TPR)=0.25, middle M=1.2, P=0.84, TPR=0.39, bottom M=0.0053 (others meaningless).

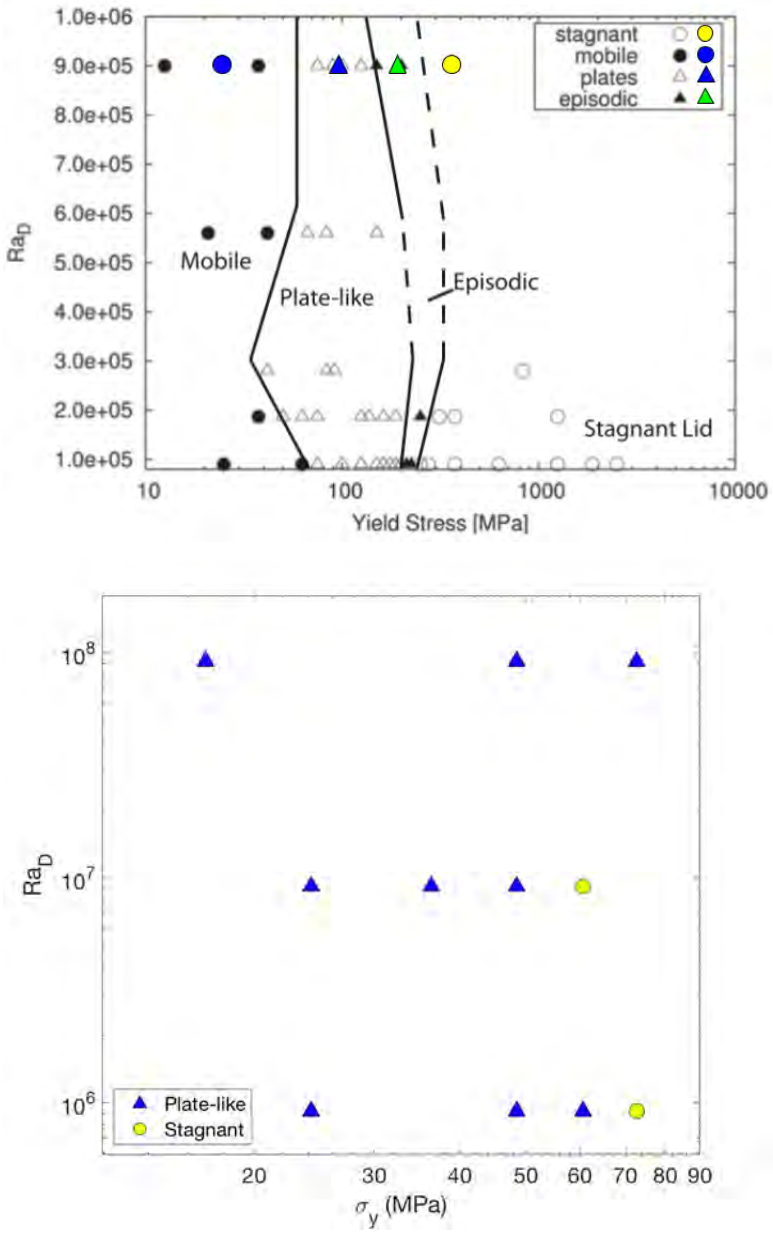

Figure 2: Rayleigh number/yield stress parameter space for $\Delta\eta = 10^4$ (top), adapted from Foley [FB09], and my results for $\Delta\eta = 10^5$ models (bottom). For $\Delta\eta = 10^4$, my results are shown in the colored symbols and line up well with Foley's results. For $\Delta\eta = 10^5$, the plate-like stagnant transition happens around 60-80 MPa and is independent of Ra. Models below 30 MPa show some characteristics of mobile behaviour, but I choose to still classify those presented as plate-like because of the visible plate boundaries and large-amplitude heat-flux behaviour.

4.2 Typical Behaviour

In Figure 3, I show the time-dependence of the surface heat flux. In steady state, each of the models heat flux oscillates around a non-dimensional value of 17, which balances the internal heat generation. This corresponds to about 13 mW/m^2, a factor of about 5 lower than Earth's 80 mW/m^2 [FB09]. This discrepancy is largely due to a thicker lithosphere than seen on the Earth (see Discussion section regarding non-linearity of the viscosity law). However, the time-dependence of the heat flow varies significantly between tectonic states. Stagnant models, whose flow is dominated by short wavelength convection and then conduction through the lithosphere, exhibit near-constant heat flow. The amplitude of the heat flux around the mean is tiny. Episodic models, by contrast, show the largest amplitude changes, with huge spikes in heat flow corresponding to the uplifting of hot mantle material to replace the cold lithosphere as it peels away. After the spike, the heat flow dips below the mean and recovers slowly. The whole mantle had been cooled by the introduction of the cold material, thereby reducing the heat flux at the surface which returns to the mean as internal heat generation warms the mantle. These findings are similar to Ref. [FB09].

Mobile models have a low amplitude around the mean because even a small negative buoyancy can cause a drip, so even minor temperature differences are ironed out quickly. Plate-like models show very non-linear heat flux variations, with an amplitude intermediate between mobile and episodic. The patterns are very time dependent, and in a manner unlike the quasi-periodic fluctuations of episodic heat flow. They show larger amplitudes and lower overall frequencies, as well as less regularity. For instance, there are quiet periods (0.03-0.04) and periods of high activity (0.045-0.07). The overall behaviour is non-linear.

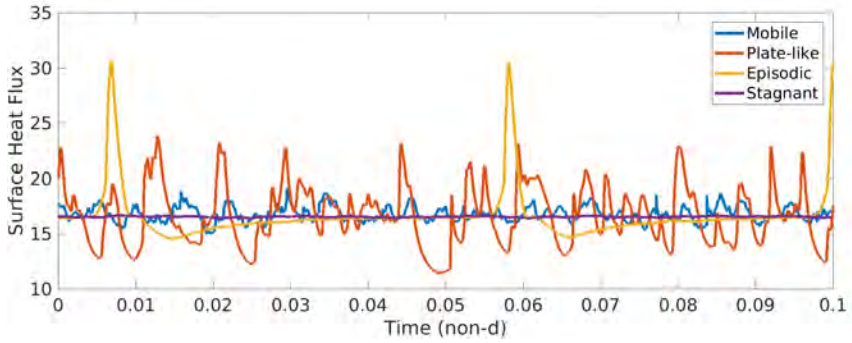

Figure 3: Time dependence of the surface heat fluxes of four models with $\Delta\eta = 10^4$, $Ra_D = 10^6$ in steady-state. The mobile model has yield stress 24 MPa, plate-like 96 MPa, episodic 192 MPa, and stagnant 384 MPa. A non-dimensional time of 0.05 scales to 64 Ga. A surface heat flux of 17 scales to 13 mW/m^2, balancing 7 TW internal heat production.

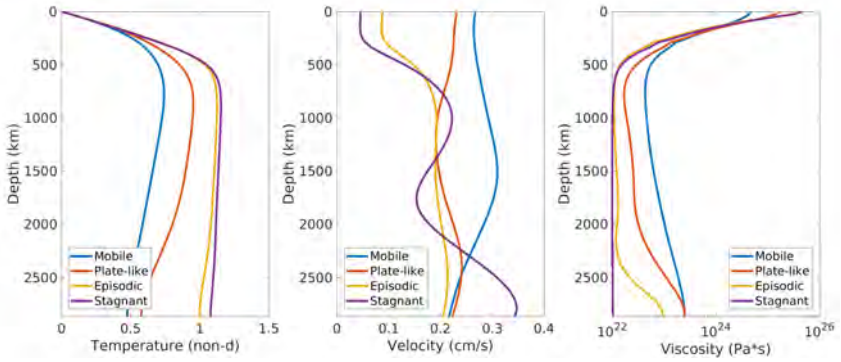

Figure 4: Time-averaged temperature, root-mean square velocity, and viscosity horizontally-averaged depth profiles for the same models in Fig. 3 above. Mobile and plate-like models experience a warm mid-mantle, a product of cool material from the surface bypassing, and not stagnating at, intermediate depths. Instead the material falls straight to the CMB, at once cooling the base and pushing mid-mantle material, which had time to warm unaffected, higher. The temperature curve for the stagnant model very clearly shows the transition from conduction-dominated (low velocity, linear temperature gradient) to advection-dominated heat transport (no temperature gradient) at 500 km depth. Episodic models mix characteristics from stagnant and plate-like models.

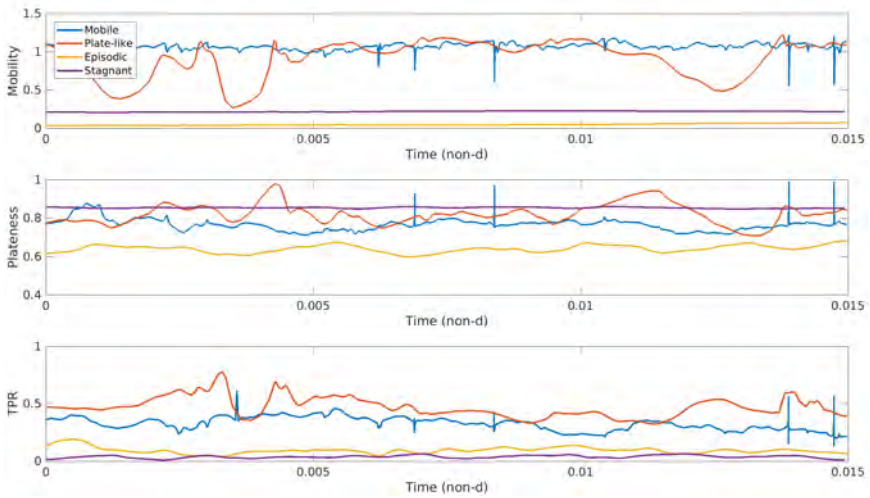

Figure 5: Time-dependent behaviour of a set of models in all tectonic states ($\Delta\eta = 10^4$, $Ra_D = 10^6$). The episodic behaviour of the yellow line is hidden by the short time window. A time of 0.015 corresponds to 19 Ga.

The nature of the time dependence of these metrics in Figure 5 is some-

what more opaque. The mobile models show relatively constant mobility, plateness, and TPR, but with sharp spikes of activity corresponding to sudden drips and velocity changes. In fact, the only model which shows significant time-dependence of the mobility on this short timescale is the plate-like model, which has several long periods of reduced mobility. The episodic model shows large swings over a longer timescale. The plateness values of the stagnant model, although high, are meaningless in this context since there is very little overall strain rate at the stagnant surface.

4.3 Effect of Viscosity Contrast

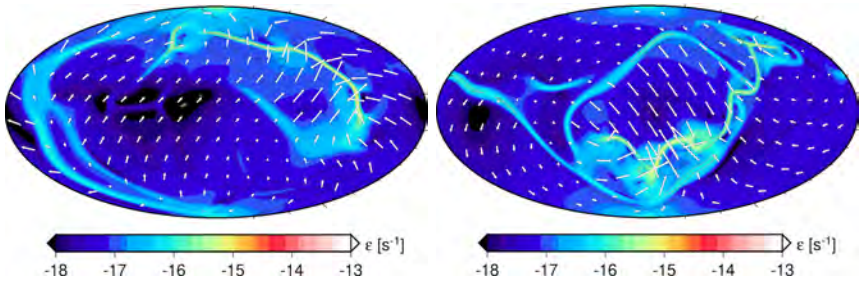

Figure 6: Surface strain rate of two plate-like models ($Ra_D = 10^6$) for viscosity contrasts of 10^4 (left) and 10^5 (right)

On a qualitative level, the plate-like models improve with increased viscosity contrast. Plate boundaries, especially convergent ones, are narrower and more sharply defined, with large velocity gradients. Instead, only larger ranges of viscosities allow large parts of the surface to remain intact while the deformation occurs over a smaller linear scale. The area of deformation does not differ dramatically (see similar plateness values in Fig. 7), however, Figure 6 shows that the surface has smaller plates.

Figure 7 shows the time averages of a set of metrics and their standard deviations. The yield stress of the transition from plate-like to stagnant decreases to 60 MPa from 150 MPa, showing a displacement in the temperatures and other metrics. The velocities are overall lower in the $\Delta\eta = 10^5$ case, but the mobility and plateness increase. However, TPR values remain constant.

Figures 8 and 9 show the surface toroidal and poloidal powers and TPR values, respectively, as a function of convective degree. TPR decreases as a function of degree after peaking in degree 2. However, TPR is overall higher for the lower viscosity contrast $\Delta\eta = 10^4$. Additionally, the total power decreases as a function of viscosity contrast.

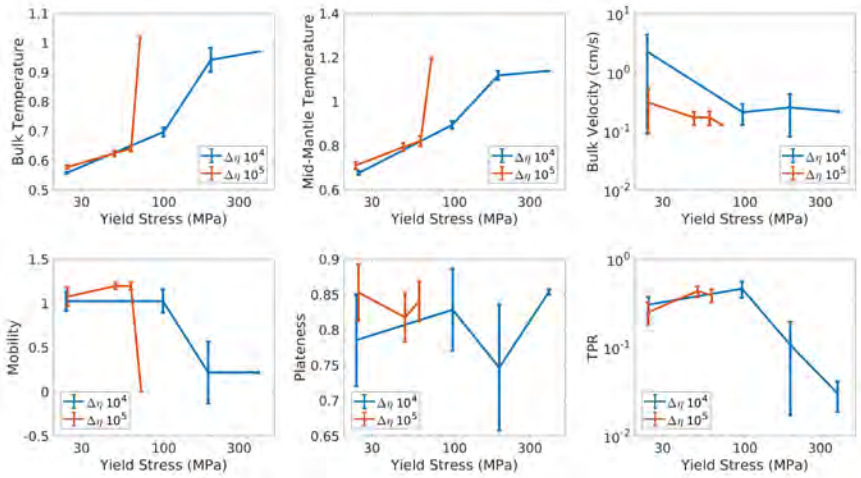

Figure 7: Time averages of several metrics: the bulk averaged temperature, the mid-mantle temperature, root-mean-square velocity, and mobility, plateness, and TPR. The error bars correspond to one standard deviation. The values are shown as a function of yield stress and viscosity contrast for models at $Ra_D = 10^6$. The yield stress values are perturbed slightly to give better visibility where the values overlap. Missing data ($\Delta\eta = 10^5$, stagnant, at 92 MPa), in the bottom middle and right plots only, are not plotted.

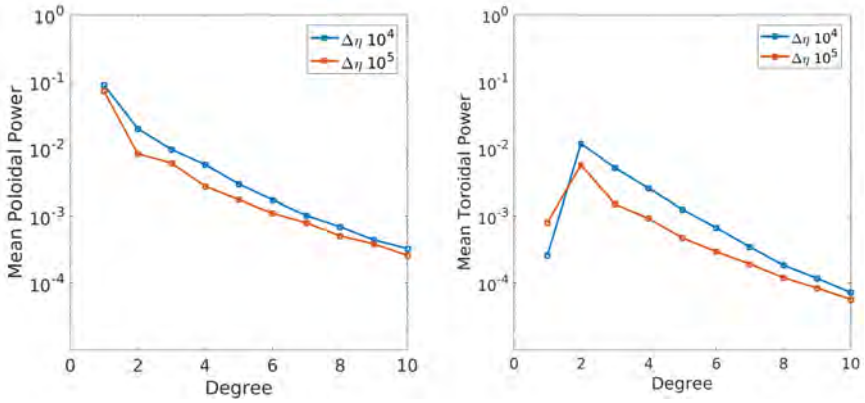

Figure 8: Mean surface poloidal (left) and toroidal (right) powers as a function of degree for degrees 1-10, for plate-like models as a function of $\Delta\eta$ at $Ra_D = 10^6$. Toroidal power is lower than poloidal power overall by a factor of around 5-7. Poloidal fields show a monotonic decrease in power as a function of degree, while toroidal fields peak in degree 2. The total power decreases as a function of viscosity contrast because of the decrease in overall velocity (see Fig. 7).

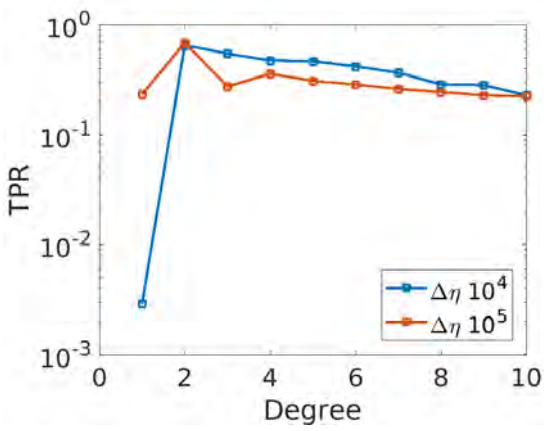

Figure 9: Surface TPR as a function of degree for degrees 1-10, for plate-like models as a function of $\Delta\eta$ at $Ra_D = 10^6$. TPR decreases as a function of degree after peaking in degree 2.

4.4 Effect of Rayleigh Number at High Viscosity Contrast

In this section, I present results concerning the effect of the high Rayleigh number on the convection patterns of these models at $\Delta\eta = 10^5$. The three mantle Rayleigh numbers (Ra_D considered are 9×10^5, 9×10^6, and 9×10^7, which I denote 10^6, 10^7, and 10^8 for brevity.

In Fig. 10, we see that the Rayleigh number has an important effect on the surface expression of flow. Increased Ra sharpens the plate boundaries and fractures the surface into more plate-like regions. The higher convective vigor has more small-wavelength flow and so generates fine structure on the surface.

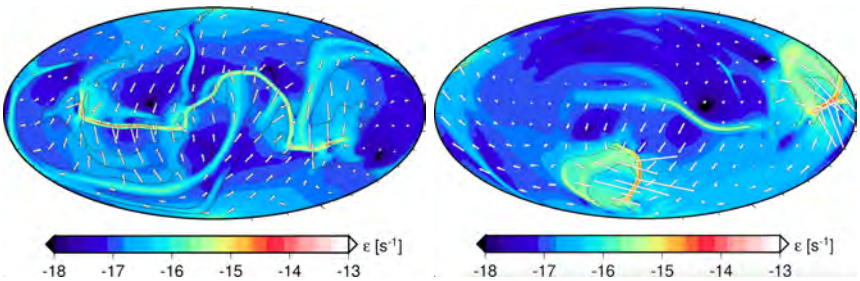

Figure 10: The surface strain rate for two plate-like models ($\Delta\eta = 10^5$, $\sigma_y = 48$ MPa) at $Ra_D = 10^7$ (left) and $Ra_D = 10^8$ (right). The higher Ra_D model on the right shows shorter plate boundaries which roll forward and peel off slices of the lithosphere, unlike the large sheet-like downwellings seen on the real Earth.

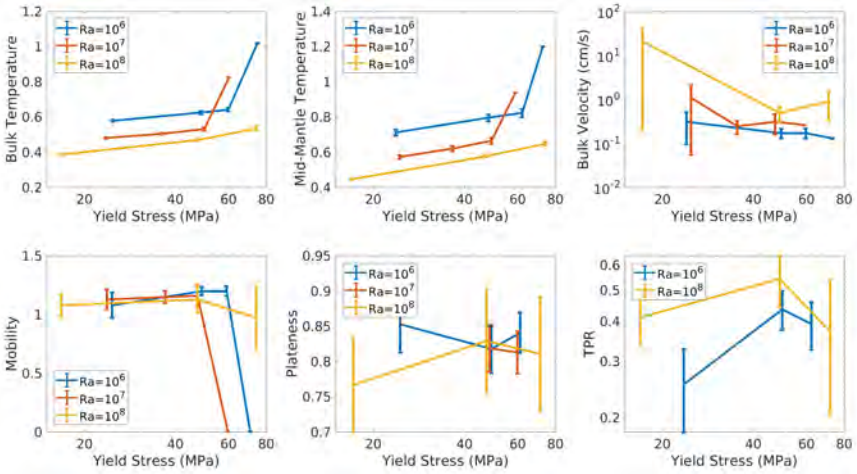

Figure 11: Time averages of a range of metrics. The error bars correspond to one standard deviation. The values are shown as a function of yield stress and mantle Rayleigh number at viscosity contrast 10^5. The yield stress values are perturbed slightly to give better visibility where the values overlap. Missing data in the bottom middle and right plots are not plotted. The bottom set of figures show that the mobility does not change with increased Rayleigh number, while the TPR increases. The plateness does not show a significant trend up or down. Additionally, the $Ra = 10^8$ models show large standard deviations across all metrics.

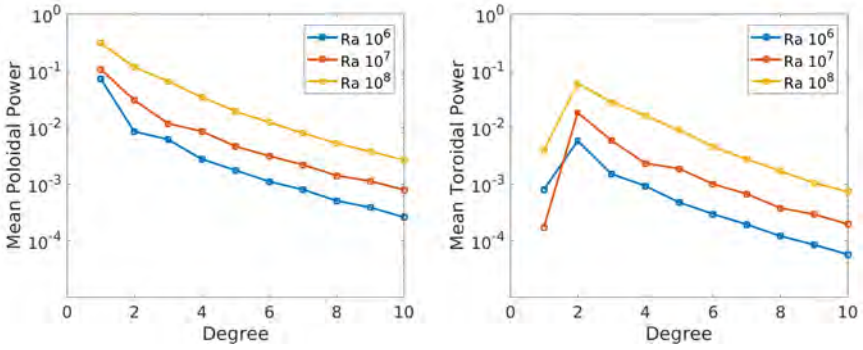

Figure 12: Mean surface poloidal (left) and toroidal (right) powers as a function of degree for degrees 1-10, at high viscosity contrast and as a function of Rayleigh number. Toroidal power is lower than poloidal power overall by a factor of around 7. Poloidal fields show a monotonic decrease in power as a function of degree, while toroidal fields peak in degree 2. Power increases across the spectrum as a function of Rayleigh number, a function of the increased overall velocity (see Fig. 11 above).

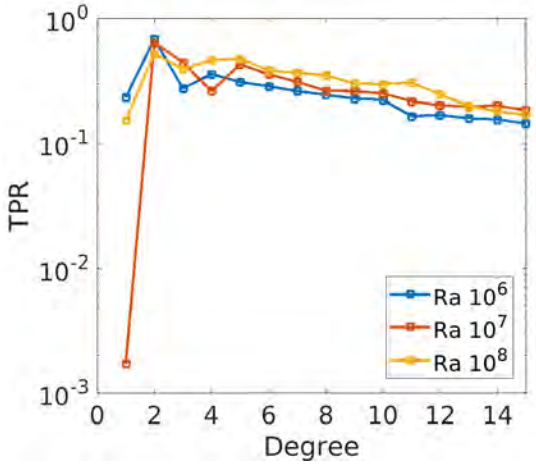

Figure 13: Surface TPR as a function of degree for degrees 1-10, at high viscosity contrast and as a function of Rayleigh number. TPR decreases as a function of degree after peaking in degree 2. TPR increases as a function of Ra by around a factor of 1.2-1.5 for each factor of 10 Ra increase, at degrees greater than 5. Degrees 3 and 4 show reduced TPR compared to degree 2.

In Fig. 11, I show the temporal averages of the metrics as a function of Rayleigh number. As Ra increases, corresponding increases in velocity cause the temperature to drop. The mobility remains practically constant. The plateness does not seem to change greatly from 0.8. However, TPR increases significantly, reaching the Earth-like values of 0.5-0.6 [A R+93]. The highest Rayleigh number also shows significant increases in the standard deviation of all metrics.

Figs. 12 and 9 display the toroidal-poloidal powers and TPR as a function of convective degree. The increase in velocity increased the total power overall as a function of Rayleigh number. The TPR did not show such a coherent change, but at high degrees, the TPR increased as a function of degree. TPR increases as a function of Ra by around a factor of 1.2-1.5 for each factor of 10 Ra increase, at degrees greater than 5. Degrees 3 and 4 show reduced TPR compared to degree 2.

4.5 Resolution Test

For each model in the $\Delta\eta = 10^4$ viscosity contrast ($Ra = 10^6$) case, I ran two identical models with differing resolutions, one at $64^3 \times 12$ and one at $128^3 \times 12$ volumes. I compare the time-dependence of the surface heat flux in Fig. 14. For both the mobile and the plate-like case, the solutions begin to diverge quickly, a natural effect of the non-linear nature of the convection code, seen also in Foley et al [FB09]. However, the metric averages show little to no change (Fig. 15), indicating the models are statistically identical.

I conclude that $128^3 \times 12$, which I used in all other models, is an appropriate

resolution. Although I have not yet run a high-resolution test at the highest Ra and $\Delta\eta$ (see Discussion section), I saw no evidence of characteristic numerical glitches in the velocity fields, which show up as diamond patterns following the cap structure and which indicate numerical failure.

Future work could improve understanding by analyzing the statistical properties of the two flows after they reached steady-state. Specifically, one can compare the amplitude, shape, and frequency of the oscillations of the heat flux using Fourier transforms.

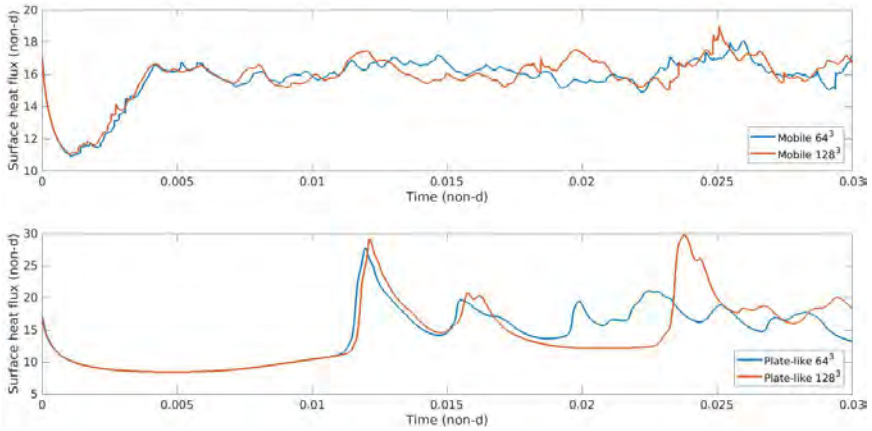

Figure 14: Surface heat flux compared between mobile (top) and plate-like (bottom) models with $64^3 \times 12$ and $128^3 \times 12$ resolution. A time of 0.03 corresponds to 38 Ga. The mobile models diverge sooner and are uncorrelated by around 0.01, while the plate-like models lose coherence around time 0.02.

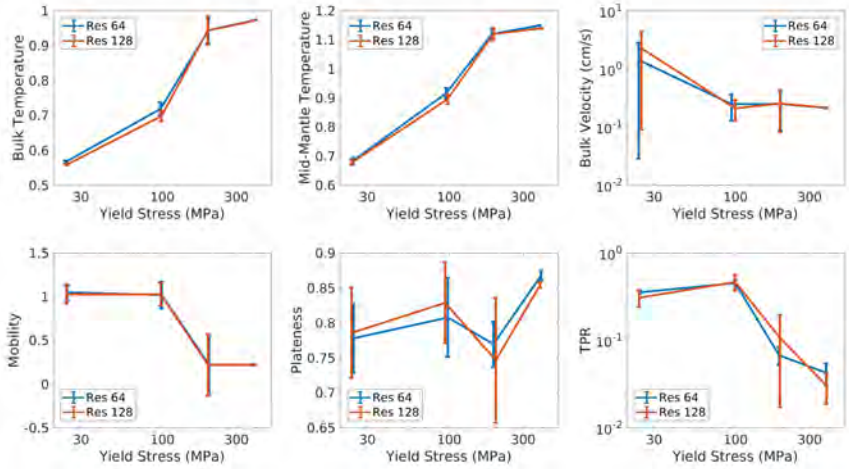

Figure 15: Comparison of model metric averages for low ($64^3 \times 12$ volumes) and high resolution ($128^3 \times 12$ volumes) at $Ra_D = 10^6$. There is very little change overall, indicating that at least the low resolution models are statistically indentical across resolution. The high resolution models are slightly cooler and in mobile and plate-like cases show improved fractionally improved plateness by around 1-3%.

5 Discussion

Overall, this work is a step towards self-consistent generation of Earth-style plate tectonics in models. Simply increasing the Rayleigh number to Earth-like values gives considerable improvement compared to previous models in the TPR values and surface structure. Perhaps this result is not surprising, but it confirms that to generate appropriate behaviour similar to the Earth, one must start with a model with the correct Rayleigh number. The viscosity contrast is also important, but remains below realistic values.

My models lack many important components of the real-Earth system in an effort to study basic convection. I do not include continents, for instance, although there is evidence to suggest that they improve degree-2 convection [Zho+07b].

I find no episodic models at a high viscosity contrast. The episodic regime is less stable of a state than the others, and more of a chaotic oscillation between the plate-like and stagnant states. At higher viscosity contrasts, the range of this meta-stable episodic behaviour narrows to the point of being invisible.

5.1 Future Work

I intend to do additional work to narrow down the $\Delta\eta = 10^5$ plate-like/stagnant transition, especially at high Rayleigh numbers. This will permit me to make a

definitive conclusion about the transition dependence on Ra. I will also perform an ultra-high resolution test ($256^3 \times 12$ volumes) to ensure that the highest Rayleigh number and viscosity contrast models are properly resolved at $128^3 \times 12$ volumes.

Although in this paper I present the toroidal and poloidal powers on the surface as a function of degree, a more commonly used test of the dominant degree of convection lies in the temperature field. I plan to take temperature power spectra as a function of depth, following the example of Ref [FB09]. The results from that work show the dominance of degree-1 convection for plate-like models at low viscosity contrast, where the Earth mostly runs at degree-2.

In an effort to make the viscosity laws reflect the Earth better I intend to introduce an asthenosphere, a weak layer under the lithosphere. This layer is easily visible in seismic tomography as the Mohorovicic discontinuity at 5-10 km depth in the oceans [Lov58]. It is caused by partial melting where the temperature exceeds the solidus [TP97][Was+03]. In the Earth there is also a prominent viscosity increase at 670 km [DR92][Tac00a]. In models, I will implement this effect as a pre-factor of 50 in the viscosity.

Refs [Tac00b] and [FB09] and have done work exploring depth-dependent yield stress, taking cue from the pressure-dependent activation of the yield stress [Tac00a][MS98] . Although I have not discuss that here, I and others have found improved plate-like behaviour.

I further intend to examine in detail the non-linearity of the Arrhenius viscosity law. Preliminary results have shown that mild increases in non-linearity give more plate-like surface patterns and improved metrics. However, non-linearity also exhibits control over the yield stress parameter space of plate-like motion.

All of these adjustments can be compared to the base models to determine how to improve Earth-like qualities. The plateness, the dominant degree of convection, and the surface pattern especially could show improvement towards a more Earth-like nature. Other future improvements lies in more heterogeneous models or those with rheologies which allow one-sided subduction and fault reactivation.

A promising avenue of research lies in the implementation of strain and strain damage for reactivation of old faults [FB19] into 3-D spherical models. Although this concept has existed for decades [Tac00c], the resources to explore this in a comprehensive way has just recently become available.

The imposition of continental material using the tracer ratio method [TK03], with a lighter buoyancy and stronger yield stress [Tac00c], is another fruitful area of study. Models continents have been shown to give one-sided downwellings [Tac00b] like seen on the Earth [Zha04]. In general, more processes are related to this phenomena, such as hydration of slabs [GCY08], and it is not only observed at continent-ocean interfaces. However, addition of continents would allow for study of the dynamics of the super-continental Wilson cycle [Zho+07b].

6 Conclusion

The generation of plate tectonics from mantle convection is a complex problem. In this paper I took advantage of new-found computation resources to simulate convection at Earth-like Rayleigh numbers for a whole range of models.

I confirmed mobile, plate-like, and stagnant tectonic states persist up to high Ra and viscosity contrast, but episodic models disappear at $\Delta\eta = 10^5$. The plate-like/stagnant transition seems to be independent of Rayleigh number and occurs at a constant yield stress of 60-80 MPa.

I investigated the effects of increased viscosity contrast and found higher velocities and generally higher mobility and plateness. The higher viscosity contrast showed plate-like behaviour on a reduced range of yield stress, from 10-60 MPa, compared to Foley and Becker's [FB09] 75-210 MPa.

I explored the parameter space at Rayleigh numbers within the Earth-like range. At the highest Rayleigh number, I found models with Earth-like TPR values, with averages above 0.5, and with plateness above 0.8.

I performed a resolution test on relatively low Ra and viscosity contrast models which showed excellent agreement. To that end, I consider $64^3 \times 12$ an acceptable resolution for models under $Ra_D = 10^6$, $\Delta\eta = 10^4$. However, a resolution of $128^3 \times 12$ is necessary for more intensive models.

I finally discussed a list of improvements to make to these models to bring them accurately recreate the physics and patterns observed in the real-world mantle convection.

7 Acknowledgements

I would like to thank my advisers and colleagues Lukas Fuchs and Thorsten Becker, who supported me and helped me with everything from learning the science to fixing bugs in my code. I also wish to thank the UT Institute for Geophysics and the Texas Advanced Computing Center for giving my group the resources to undertake this computationally intensive project.

References

[A R+93] Mark A. Richards et al. "Toroidal-poloidal partitioning of plate motions since 120 MA". In: *Geophysical Research Letters - GEOPHYS RES LETT* 20 (Mar. 1993). DOI: 10.1029/93GL00168.

[BB02] Thorsten W. Becker and Lapo Boschi. "A comparison of tomographic and geodynamic mantle models". In: *Geochemistry, Geophysics, Geosystems* 3.1 (2002). DOI: 10.1029/2001GC000168.

[BKI15] MD Ballmer, Peter E van Keken, and G Ito. "Hotspots, large igneous provinces, and melting anomalies". In: (2015).

[CGU17] Nicolas Coltice, Mélanie Gérault, and Martina Ulvrová. "A mantle convection perspective on global tectonics". In: *Earth-Science Reviews* 165 (2017), pp. 120–150. ISSN: 0012-8252. DOI: https://doi.org/10.1016/j.earscirev.2016.11.006. URL: http://www.sciencedirect.com/science/article/pii/S0012825216304354.

[Chr84] U Christensen. "Convection with pressure-and temperature-dependent non-Newtonian rheology". In: *Geophysical Journal International* 77.2 (1984), pp. 343–384.

[DC01] Charles R. Doering and Peter Constantin. "On upper bounds for infinite Prandtl number convection with or without rotation". In: *Journal of Mathematical Physics* 42.2 (2001), pp. 784–795. DOI: 10.1063/1.1336157. URL: https://aip.scitation.org/doi/abs/10.1063/1.1336157.

[DR92] Geoffrey F. Davies and Mark A. Richards. "Mantle Convection". In: *The Journal of Geology* 100.2 (1992), pp. 151–206. ISSN: 00221376, 15375269. URL: http://www.jstor.org/stable/30081131.

[FB09] Bradford J. Foley and Thorsten W. Becker. "Generation of plate-like behavior and mantle heterogeneity from a spherical, viscoplastic convection model". In: *Geochemistry, Geophysics, Geosystems* 10.8 (2009). ISSN: 1525-2027. DOI: 10.1029/2009GC002378.

[FB17] Claudio Faccenna and Thorsten W. Becker. "Tectonic Geodynamics". In: (2017).

[FB19] Lukas Fuchs and Thorsten W Becker. "Role of strain-dependent weakening memory on the style of mantle convection and plate boundary stability". In: *EarthArXiv. March* 28 (2019).

[GCY08] Taras V Gerya, James AD Connolly, and David A Yuen. "Why is terrestrial subduction one-sided?" In: *Geology* 36.1 (2008), pp. 43–46.

[GS92] Richard G Gordon and Seth Stein. "Global tectonics and space geodesy". In: *Science* 256.5055 (1992), pp. 333–342.

[HT08] H. J. van Heck and P. J. Tackley. "Planforms of self-consistently generated plates in 3D spherical geometry". In: *Geophysical Research Letters* 35.19 (2008). DOI: 10.1029/2008GL035190. eprint: https://agupubs.onlinelibrary.wiley.com/doi/pdf/10.1029/2008GL035190. URL: https://agupubs.onlinelibrary.wiley.com/doi/abs/10.1029/2008GL035190.

[JLM07] C Jaupart, S Labrosse, and JC Mareschal. "7.06-temperatures, heat and energy in the mantle of the earth". In: *Treatise on geophysics* 7 (2007), pp. 223–270.

[LHB08] Thorne Lay, John Hernlund, and Bruce A Buffett. "Core–mantle boundary heat flow". In: *Nature geoscience* 1.1 (2008), p. 25.

[Lov58] John F Lovering. “The nature of the Mohorovicic discontinuity”. In: *Eos, Transactions American Geophysical Union* 39.5 (1958), pp. 947–955.

[Mor+14] L. Moresi et al. *CitcomS v3.3.1 [software]*. Computational Infrastructure for Geodynamics, 2014. DOI: http://doi.org/NoDOI.

[MS98] Louis Moresi and Viatcheslav Solomatov. “Mantle convection with a brittle lithosphere: thoughts on the global tectonic styles of the Earth and Venus”. In: *Geophysical Journal International* 133.3 (1998), pp. 669–682.

[OGH91] Richard J O’Connell, Carl W Gable, and Bradford H Hager. “Toroidal-poloidal partitioning of lithospheric plate motions”. In: *Glacial Isostasy, Sea-Level and Mantle Rheology*. Springer, 1991, pp. 535–551.

[OSZ91] Masaki Ogawa, Gerald Schubert, and Abdelfattah Zebib. “Numerical simulations of three-dimensional thermal convection in a fluid with strongly temperature-dependent viscosity”. In: *Journal of fluid mechanics* 233 (1991), pp. 299–328.

[Ric07] Yanick Ricard. “Physics of Mantle Convection”. In: *Treatise on Geophysics* 7 (Dec. 2007). DOI: 10.1016/B978-044452748-6/00115-2.

[SH13] C. Stein and U. Hansen. “Arrhenius rheology versus Frank-Kamenetskii rheology—Implications for mantle dynamics”. In: *Geochemistry, Geophysics, Geosystems* 14.8 (2013), pp. 2757–2770. DOI: 10.1002/ggge.20158. eprint: https://agupubs.onlinelibrary.wiley.com/doi/pdf/10.1002/ggge.20158. URL: https://agupubs.onlinelibrary.wiley.com/doi/abs/10.1002/ggge.20158.

[Sol95] V. S. Solomatov. “Scaling of temperature- and stress-dependent viscosity convection”. In: *Physics of Fluids* 7.2 (1995), pp. 266–274. DOI: 10.1063/1.868624.

[Tac00a] Paul J. Tackley. “Mantle Convection and Plate Tectonics: Toward an Integrated Physical and Chemical Theory”. In: *Science* 288.5473 (2000), pp. 2002–2007. ISSN: 0036-8075. DOI: 10.1126/science.288.5473.2002. eprint: https://science.sciencemag.org/content/288/5473/2002.full.pdf. URL: https://science.sciencemag.org/content/288/5473/2002.

[Tac00b] Paul J. Tackley. “Self-consistent generation of tectonic plates in time-dependent, three-dimensional mantle convection simulations”. In: *Geochemistry, Geophysics, Geosystems* 1.8 (2000). DOI: 10.1029/2000GC000036.

[Tac00c] Paul J. Tackley. “Self-consistent generation of tectonic plates in time-dependent, three-dimensional mantle convection simulations: 2. Strain weakening and asthenosphere”. In: *Geochemistry, Geophysics, Geosystems* 1.8 (2000). DOI: 10.1029/2000GC000043.

[TK03] Paul J Tackley and Scott D King. "Testing the tracer ratio method for modeling active compositional fields in mantle convection simulations". In: *Geochemistry, Geophysics, Geosystems* 4.4 (2003).

[TP97] Hans Thybo and E Perchuć. "The seismic 8 discontinuity and partial melting in continental mantle". In: *Science* 275.5306 (1997), pp. 1626–1629.

[Wan04] Xiaoming Wang. "Infinite Prandtl number limit of Rayleigh-Bénard convection". In: *Communications on Pure and Applied Mathematics* 57.10 (2004), pp. 1265–1282. DOI: 10.1002/cpa.3047. eprint: https://onlinelibrary.wiley.com/doi/pdf/10.1002/cpa.3047. URL: https://onlinelibrary.wiley.com/doi/abs/10.1002/cpa.3047.

[Was+03] Laura E Wasylenki et al. "Near-solidus melting of the shallow upper mantle: partial melting experiments on depleted peridotite". In: *Journal of Petrology* 44.7 (2003), pp. 1163–1191.

[WL12] MB Weller and A Lenardic. "Hysteresis in mantle convection: Plate tectonics systems". In: *Geophysical Research Letters* 39.10 (2012).

[ZGM98] Shijie Zhong, Michael Gurnis, and Louis Moresi. "Role of faults, nonlinear rheology, and viscosity structure in generating plates from instantaneous mantle flow models". In: *Journal of Geophysical Research: Solid Earth* 103.B7 (1998), pp. 15255–15268. DOI: 10.1029/98JB00605. eprint: https://agupubs.onlinelibrary.wiley.com/doi/pdf/10.1029/98JB00605. URL: https://agupubs.onlinelibrary.wiley.com/doi/abs/10.1029/98JB00605.

[Zha04] Dapeng Zhao. "Global tomographic images of mantle plumes and subducting slabs: insight into deep Earth dynamics". In: *Physics of the Earth and Planetary Interiors* 146.1-2 (2004), pp. 3–34.

[Zho+07a] Shijie Zhong et al. "Numerical methods for mantle convection". In: *Treatise on Geophysics* 7 (2007), pp. 227–252.

[Zho+07b] Shijie Zhong et al. "Supercontinent cycles, true polar wander, and very long-wavelength mantle convection". In: *Earth and Planetary Science Letters* 261.3-4 (2007), pp. 551–564.